Non-invasive perturbations of intracellular flow reveal physical principles of cell organization

Matthäus Mittasch[1,2], Peter Gross[3], Michael Nestler[4], Anatol W. Fritsch [1,2], Christiane Iserman[1], Mrityunjoy Kar[1,2], Matthias Munder[1], Axel Voigt[2,4], Simon Alberti[1], Stephan W. Grill[2,3] and Moritz Kreysing [1,2]*

Recent advances in cell biology enable precise molecular perturbations. The spatiotemporal organization of cells and organisms, however, also depends on physical processes such as diffusion or cytoplasmic flows, and strategies to perturb physical transport inside cells are not yet available. Here, we demonstrate focused-light-induced cytoplasmic streaming (FLUCS). FLUCS is local, directional, dynamic, probe-free, physiological, and is even applicable through rigid egg shells or cell walls. We explain FLUCS via time-dependent modelling of thermoviscous flows. Using FLUCS, we demonstrate that cytoplasmic flows drive partitioning-defective protein (PAR) polarization in *Caenorhabditis elegans* zygotes, and that cortical flows are sufficient to transport PAR domains and invert PAR polarity. In addition, we find that asymmetric cell division is a binary decision based on gradually varying PAR polarization states. Furthermore, the use of FLUCS for active microrheology revealed a metabolically induced fluid-to-solid transition of the yeast cytoplasm. Our findings establish how a wide range of transport-dependent models of cellular organization become testable by FLUCS.

Physical transport processes inside cells, such as diffusion[1,2] or cytoplasmic flows[3,4], are widely believed to be essential for animal development[5] and cellular homeostasis[6,7]. Examples of these are the diffusion of proteins and metabolites through the cytoplasm[8–12], active cytoplasmic streaming[3,4], as well as cortically induced advective flows[13,14] during cell polarization[15–17]. Despite their hypothesized importance in a wide range of cellular systems, it has so far rarely been possible to confirm the physiological significance of these physical transport processes, which is largely due to a lack of suitable perturbation methods. Genetic perturbations allow us to systematically dissect the molecular level of cellular organization, but we currently do not have suitable tools to study the causal implications of intracellular transport. As an example, how would one change the direction, velocity or temporal persistence of cytoplasmic flows to study their role during zygote polarization[17]? This would be extremely challenging using genetics, and bears the risk of introducing unspecific side effects. As a result of this methodological shortcoming, our insights into the physiology of intracellular flows often remain at a purely correlative level. Therefore, it remains controversial whether cytoplasmic motion[7,18–20] and flows[3,4] are only unspecific by-products of energy-consuming machinery, or indeed are functional and under cellular control.

To understand cellular organization in space and time, we therefore need to go beyond genetic and chemical perturbations and find ways to actively probe the role of intracellular transport as a physical driver of biochemical patterning and homeostasis. To this end, we report on a set of conceptually new experiments, which reveal both the causes and consequences of intracellular transport via focused-light-induced cytoplasmic streaming (FLUCS).

Results

**Light-induced flows in cell extracts.** Previous work has shown that light-induced travelling temperature fields can induce flows in homogeneous viscous media[21,22]. When induced practically by a moving laser beam (Fig. 1a and Supplementary Fig. 1a,b), thermal expansion drives these flows from the expanding front to the contracting wake of the heating beam (Fig. 1b). Complemented by expansion and contraction at the beginning and end of each scan period, this yields net flows (Fig. 1b). To assess the suitability of this physical effect (Fig. 1b) to drive flows with small temperature amplitudes (Fig. 1c, Supplementary Fig. 1c–e and Supplementary Video 1) in cells and developing organisms, we first experimentally checked its compatibility with crowded cytoplasmic media. Using a microscope tailored to the physiological and optical needs of biological samples (Supplementary Methods), we find that even long-range directed flows can be induced in molecularly dense *Xenopus laevis* egg extracts (Supplementary Figs. 2 and 4 and Supplementary Video 2). This finding makes thermoviscous flows particularly interesting to investigate the role of transport in morphogenetic systems, which naturally depend on advective transport through crowded cellular environments.

Control of cytoplasmic motion in *Caenorhabditis elegans* zygotes. A widely studied model system is the nematode worm *C. elegans*. During its early development, actively driven intracellular transport processes have been suggested to be relevant for a broad range of morphogenetic events. Using thermoviscous pumping, we find that the cytoplasm of this zygote responds as a fluid (Fig. 1b,d and Supplementary Video 3), unconstrained in its ability to follow flow stimuli. At temperature waves of only $\Delta T = \pm 3\,K$ (cooling achieved by global temperature reduction, Supplementary Fig. 1c–e and Supplementary Video 4), the induced flows already exceed wild-type velocities[14] by a factor of two. Importantly, control assays showed no temperature-induced developmental changes (Supplementary Fig. 3 and Supplementary Video 5), in line with the much wider range of viable and reproduction temperatures (11–26 °C)[23]. Similarly,
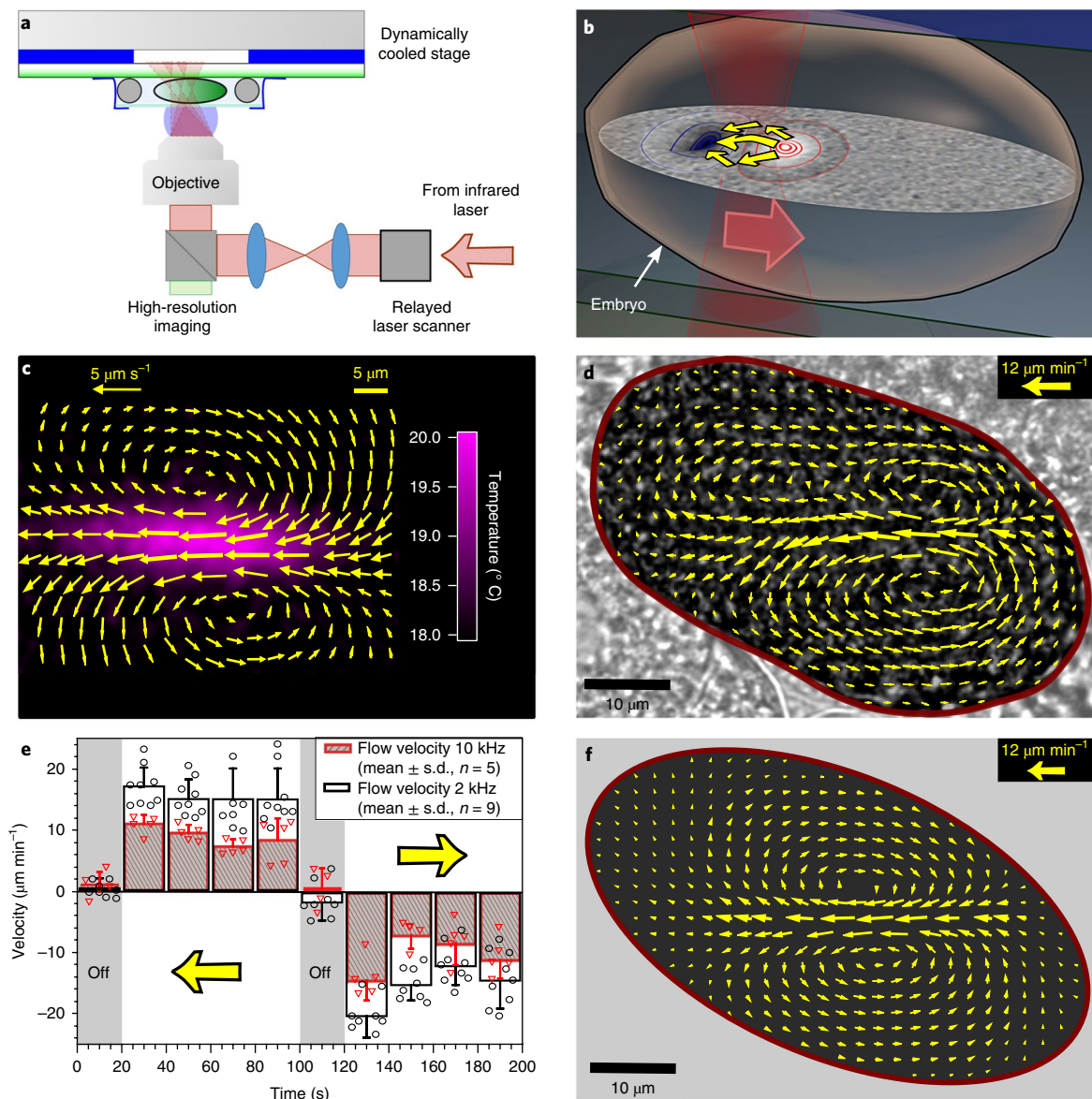
Fig. 1 | FLUCS inside *C. elegans* embryos. a, Schematic depicting the custom-built intracellular microfluidics device. A scanning infrared laser beam is coupled into the back-focal plane (BFP) of a high-numerical-aperture custom-coated microscope objective lens, allowing for simultaneous high-sensitivity fluorescence imaging and local, dynamic induction of micrometre-scale hydrodynamic flows. Heat management is achieved by a combination of highly conductive sapphire slides and PID-controlled Peltier elements, enabling rapid active adjustment of temperature on the slide. **b**, Concept: laser-induced, low-amplitude temperature waves give rise to cytoplasmic flows within cells and living embryos. These arise due to the combination of thermoviscous flows across the moving laser beam and source–sink-type flow fields resulting from its spatial modulation (see text and Supplementary Fig. 5a,b for physical details). **c**, Example of a flow field in a water–glycerol mixture at laser repetition rates of 2 kHz (34 similar replicates were performed). **d,e** Flows induced in an intact *C. elegans* zygote using temperature oscillations of ±3 K (**d**) and quantification (**e**) (data represent mean ± s.d. for *N* biologically independent embryos). The flows are directed, dynamic and well in excess of wild-type flows. **f**, Fully determined three-dimensional simulation of flows induced in an embryo-like geometry shows good agreement with measured flows in **d** (see Fig. 2 for simulation details).

sensitive heat-stress response assays in cultured cells were negative (Supplementary Fig. 3). The non-invasive character of the induced flows is further highlighted by their compatibility with there being an intact egg shell. Studying these induced intra-embryonic flows in more detail, we find them to be precisely controllable with regard to (1) temporal dynamics, (2) directionality and (3) spatial localization, both within the one-cell zygote and at later blastomere stages (Fig. 1e, Supplementary Video 3 and Supplementary Fig. 4c–e).

Induced flows match theoretical description. To confirm that these flow fields are consistent with a physical description, we

inserted experimental parameters such as scan frequency, temperature profile and thermal response coefficients for cytoplasmic water into a theoretical model. We extended previous modelling of thermoviscous flows[21,22] to also account for temporal changes in laser intensity along the path (Fig. 2 and Supplementary Fig. 5a–d). This extension introduces a second source term, which is required to account for the limited laser scan paths in confined volumes (Fig. 2a). Together with the thermoviscous flows, this yields the experimentally observed net flows. This time-dependent version of the Stokes equation was numerically solved in a three-dimensional embryo-resembling geometry (Fig. 2b,c), using a finite-element
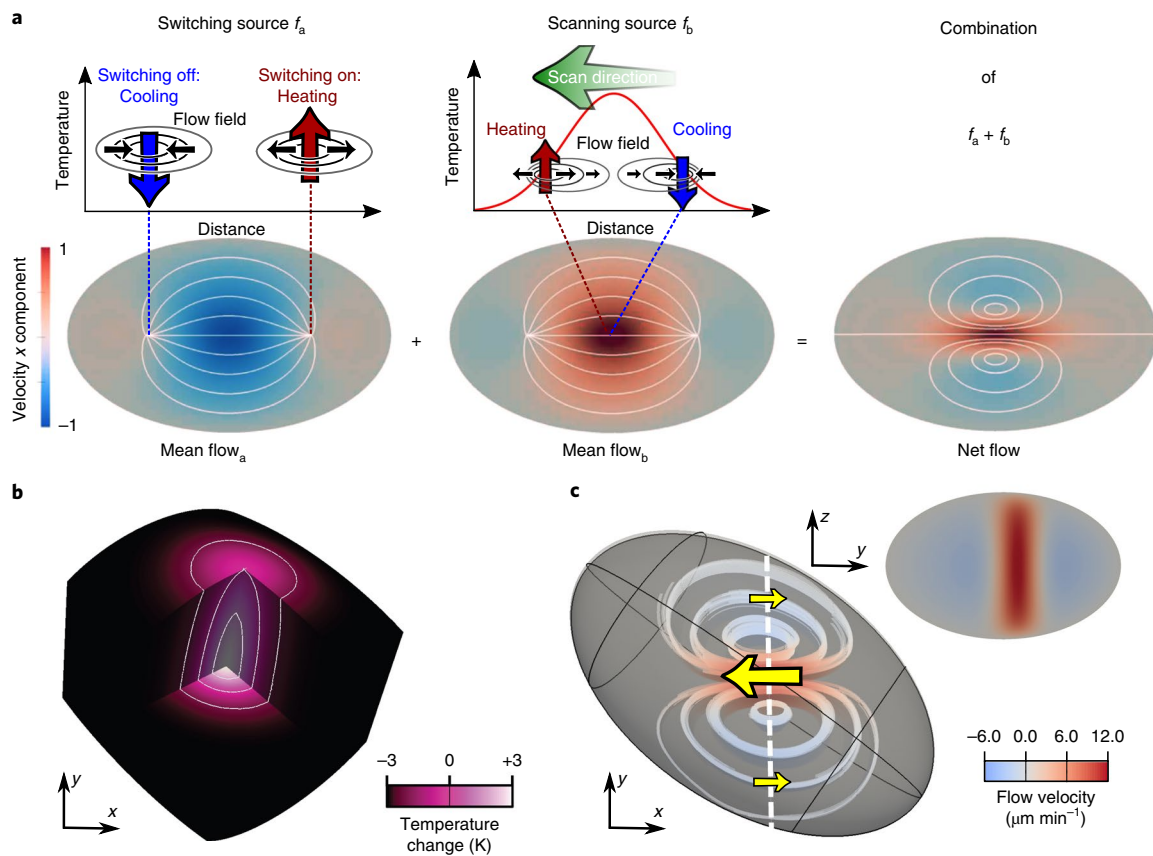
Fig. 2 | Physical modelling of induced cytoplasmic flows. a, In confined cellular geometries, induced cytoplasmic flows arise due to changes in the temperature profile along the laser scan path (source f_a), as well as thermoviscous expansion across the moving laser beam (source f_b). In combination, the two flow sources yield the time-averaged and experimentally observed net flows. **b**, Distribution of instantaneous temperature increase in a three-dimensional section of the computational embryo-like domain. **c**, Streamlined representation revealing three-dimensional modulation of the simulated intra-embryonic flow field. The cross-section is taken along the dashed white line. Numerical quality was tested using various standard approaches (Taylor-Hood elements).

simulation environment (AMDIS[24,25]). Remarkably, without applying fitting parameters, flow fields obtained from this fundamental physical approach closely match experimental observations, including absolute velocities (compare Fig. 1d,f). This implies that, despite its complex composition, the material properties of the *C. elegans* zygote cytoplasm can be described by a viscous fluid with a thermal response near or identical to that of water. Our theoretical model further reveals that temperature-induced flows and wild-type intracellular flows share the important physical characteristic of being divergence- and net-force-free. We therefore conclude that the high degree of spatiotemporal control, their physical nature and tractability by theory, render intracellular flow perturbations highly suitable for the study of the causal role of physical transport processes inside cells. We suggest that this experimental strategy to induce flows in cells and embryos be referred to as FLUCS (focused light-induced cytoplasmic streaming).

Probing the functional role of intracellular transport during PAR polarization. A central morphogenetic event at the onset of *C. elegans* development is polarization of the zygote prior to its asymmetric division into differently sized daughter cells. It has been suggested that, during polarization, cortex-driven flows act as a primary physical driver for partitioning-defective proteins (PARs) to localize at opposite poles of the embryo[16,17,26]. However, showing the causal relation between flows and polarization remains a challenge because of the vital importance of an intact cytoskeleton (which is heavily compromised when trying to reduce flows genetically)

and also the presence of a flow-independent rescue chain via PAR–microtubule interactions[27].

Cytoplasmic flows enhance cortical loading of PARs. To systematically dissect the causal roles of flows during PAR polarization, we studied the consequences of dynamically introduced, distinct flow modes in the *C. elegans* zygote. First, we investigated whether cytoplasmic flows directed towards the establishing posterior pole, as they also occur during the wild-type polarization process, drive PAR-2 loading onto the posterior membrane. For this we induced cytoplasmic flows perpendicular to the posterior PAR-2 domain (Fig. 3a and Supplementary Fig. 4f), at a speed of 7–10 μm min^{-1} (Fig. 3b), which is only about twice as fast as the wild-type cytoplasmic flows that occur downstream of cortical mobility[14,28]. As a result, we observed that the PAR-2 concentration on the membrane increased continuously up to a factor of three in less than 3 min (Fig. 3c–e and Supplementary Video 6). This well-controlled hydrodynamic perturbation demonstrates that cytoplasmic flows are capable of changing PAR-2 concentrations in cells, and further suggests that during wild-type polarization, cytoplasmic flows of similar magnitude also enhance diffusive loading to the membrane.

Control over cortical flows allows PAR domains to be repositioned. Second, we addressed whether cortical flows are indeed capable of translocating membrane-bound PAR proteins to establish the anterior–posterior (AP) body axis. For this we carried out intracellular flow perturbations in the 7 min time window after
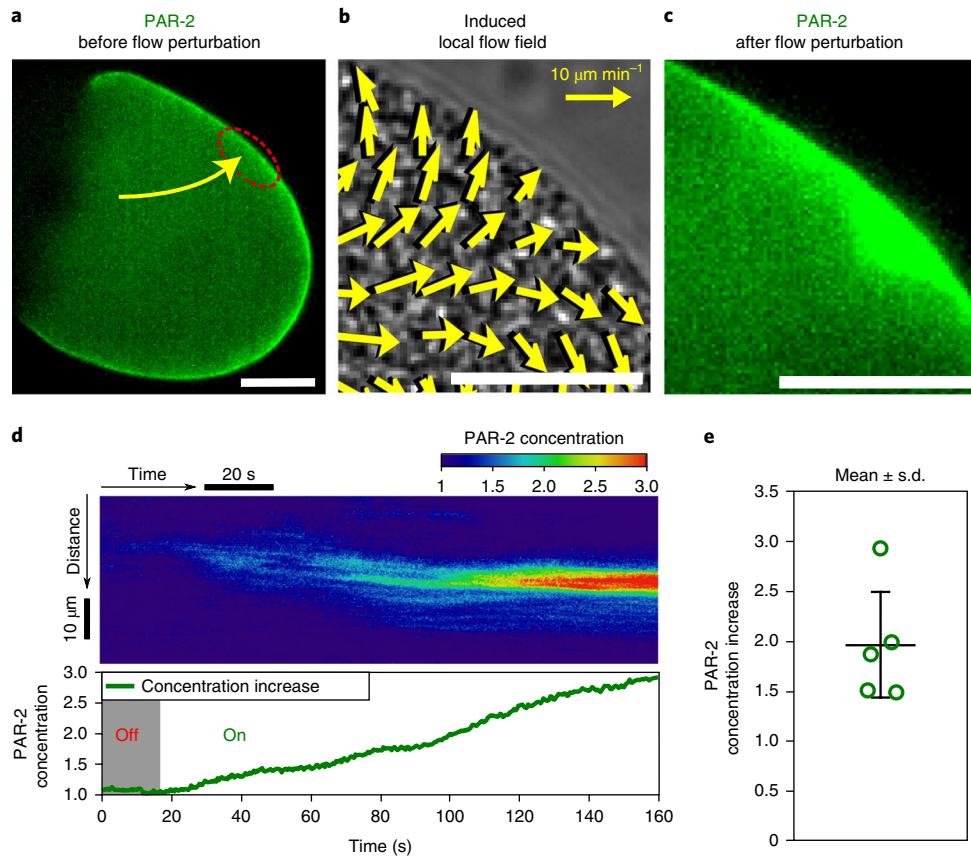
Fig. 3 | Cytoplasmic flows enhance PAR-2 loading onto the membrane. a–c, PAR-2 distribution before flow perturbation (**a**), detailed local velocity map during induction of cytoplasmic flows (**b**) and PAR-2 increase after flow stimulus (**c**). **d**, Kymographic quantification showing a threefold increase in PAR-2 concentration on the membrane in 160 s. **e**, Significant PAR-2 concentration increases at the membrane were observed in 5 out of 5 similar experiments (data represent mean ± s.d.). All scale bars, 10 μm.
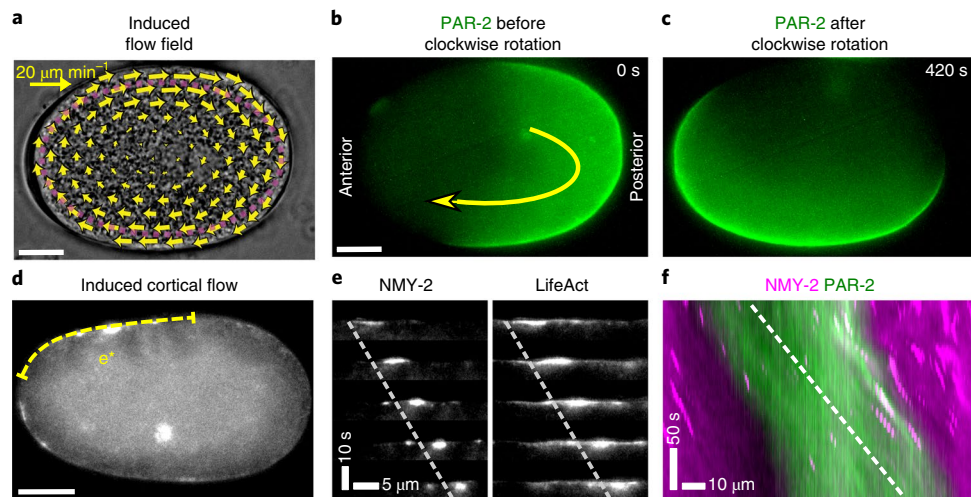
Fig. 4 | FLUCS demonstrates sufficiency of cortical flows to translocate PAR domains. a, Induced intracellular flow field (red line: laser scan path). **b,c**, Pre-established polarization of *C. elegans* zygote marked by GFP–PAR-2 before (**b**) and after 7 min (**c**) of flow perturbation. Flow-induced rotation of PAR domains, as shown in **a–c**, was similarly observed in 22 biologically independent embryos. **d–f**, Mechanism. Induced cytoplasmic flows viscously couple to and translocate the actomyosin cortex (**d**), within which myosin (GFP–NMY-2) and actin (mKate2–LifeAct) are found to move in a highly correlated manner (**e**, similar observations were made in three biologically independent embryos). e* in **d** denotes the line along which the kymographs in **e** were measured. The kymograph in **f** shows the translocation of PAR-2 (green) with the moving cortex (magenta), demonstrating the sufficiency of purely physical cortical flows to transport PAR domains. The dotted line in **f** indicates the velocity of the cytoplasm. Similar observations were made in three biologically independent embryos. Scale bars, 10 μm.
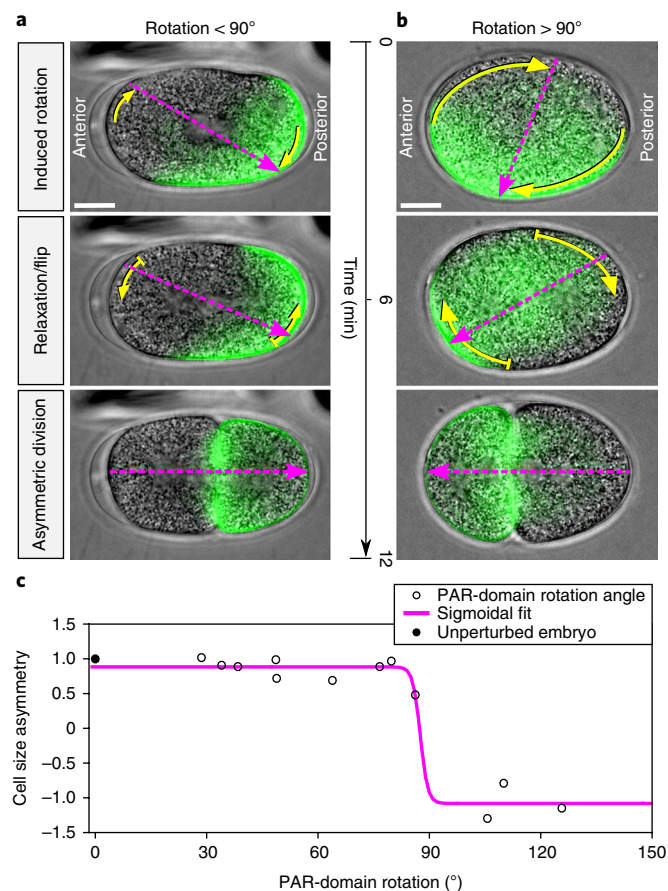
Fig. 5 | PAR rotational stability and threshold-dependent inversion of asymmetric cell division. a, In response to flow-induced rotations below 90°, PAR domains move back towards their native poles, thereby stabilizing the polarization axis during the maintenance phase and leading to stereotypical cell sizes after asymmetric division (Supplementary Video 9). **b**, For PAR domain displacements in excess of 90°, PAR domains become directed to the opposite pole, leading to an inverted PAR polarization axis and strictly inverted cell-size distributions after cytokinesis. In **a** and **b**, the pink arrows indicate the PAR-defined polarization axis; the yellow arrows indicate rotation direction of the polarized axis. **c**, Nine of nine (n) biologically independent embryos with rotation angles below 90° divided with normal asymmetry, as shown in **a**, and three of three (n) biologically independent embryos with rotation angles larger than 90° show the phenotype of an inverted cell-size ratio, as shown in **b**. Angle-dependent phenotypes are well described by threshold-dependent binary statistics (magenta line is a sigmoidal fit). Critical angle $= 87.5 \pm 1.5°$, $R^2 = 0.97$. Scale bars, 10 μm.

establishment of PAR domains (Fig. 4a), when wild-type flows mostly ceased, but before cytokinesis. We found that pre-established PAR domains follow the induced flow patterns instantaneously, and without noticeable changes in their size (Fig. 4b,c and Supplementary Video 7). Quantitative analysis of the data reveals coupling efficiencies between cytoplasmic motion and PAR domain translocation of 0.51 ± 0.14 (mean $\pm$ s.d., $n = 6$, coupling determined by the ratio of the PAR-domain and cytoplasmic velocities; see equation (1) in the Methods). We then asked how induced flows alter the polarization state of a zygote. Specifically, we tested whether the observed translocation of PAR domains, although primarily driven by flows in the cytoplasm, functions through flows of the actomyosin cortex. For this we tracked cortical flows via actin and myosin markers (mKate2-LifeAct, GFP-NMY-2). We found that induced cytoplasmic flows are capable of moving the entire

actomyosin cortex (Fig. 4d,e), even facilitating its rotation (Supplementary Video 8). Kymograph analysis (Fig. 4e) further revealed that actin and myosin move in a highly correlated manner. Whereas in the wild-type scenario cortical flows induce cytoplasmic flows (Supplementary Fig. 5e–j), here we found that this hydrodynamic coupling also works in the reverse direction, from the cytoplasm to the cortex (coupling efficiencies of 0.59 ± 0.04, mean $\pm$ s.d., $n = 3$, determined by the ratio of cortical versus cytoplasmic velocities). Taken together, near-identical coupling efficiencies of cytoplasmic flows to PAR domains and the cortex indicate a high susceptibility of membrane-bound PARs to cortical flows. The strict co-displacement of PARs with the cortex was confirmed in embryos containing both labelled PAR-2 and NMY-2 (Fig. 4f). We thus conclude that physical flows of the actomyosin cortex alone are sufficient to translocate PAR domains along the membrane.

PAR polarization shows stability against rotations up to 90°. We then asked if cortical flow speeds of physiological magnitude are sufficient to permanently alter the polarization state of a zygote, or if the zygote readjusts the PAR-defined body axis after flow-induced perturbations. We thus monitored the zygote's response to the rotation of PAR domains away from the cell's major axis, during the maintenance phase. These rotation experiments are in the spirit of, but complementary to, previous studies that measured the sizes of on-axis PAR domains as a function of needle-induced spindle displacement[29]. Following the FLUCS-driven rotation of PAR domains by angles smaller than 90°, we observed the zygote to counteract the external perturbations, and the PAR domains rotate back towards their initial position at the poles before the onset of cytokinesis (Fig. 5a and Supplementary Video 9). In all these cases ($n = 9$), including rotations of 65–85° ($n = 4$), zygotes afterwards divided normally, with full recovery of the polarization axis and the stereotypical size-asymmetry of anterior versus posterior cells. However, with rotation angles exceeding 90°, we found that PAR domains no longer rotate back to their original position. Instead, they become directed to the opposite pole, such that the PAR-defined AP body axis flips by 180° (Fig. 5b, $n = 3$ out of 3). As a direct gain-of-function phenotype of the flow-induced PAR inversion, we found the geometric body axis of the two-cell embryos to be inverted in all cases, with the small cell located at the former anterior pole (Fig. 5b and Supplementary Video 9).

Asymmetric cell division is a binary decision based on gradually varying polarization states. Statistical analysis of the rotation-induced two-cell phenotypes further strengthened the view of a threshold-angle-dependent inversion. Fitting cell-size asymmetry (see Methods) as a sigmoidal function of the induced rotational angle suggests that cell division remains unaffected up to rotation angles of $87.5 \pm 15°$ and then suddenly inverts for higher angles (Fig. 5c). Based on the data, we propose that PAR polarization in *C. elegans* is a process with stable domain positions around the poles, which the zygote terminally decides in a binary fashion during the process of cytokinesis, thereby leading to normal or strictly inverted cell size asymmetry. In conclusion, we have shown, by non-invasive hydrodynamic perturbations, how cell polarization, a fundamental developmental process, is driven and altered by intracellular flows of physiological magnitude. Our results stress the central importance of physical intracellular transport in morphogenetic systems, and we suggest a conceptually new route to test these.

Flow-driven active microrheology within cells. We now turn from embryogenesis to homeostasis, a second cellular characteristic for which intracellular physical transport is thought to be of high physiological relevance. In particular, it has been suggested that cells exploit physical transport through the cytoplasm as a kinetic regulator of cellular metabolism[6,7]. In yeast cells specifically, it has recently
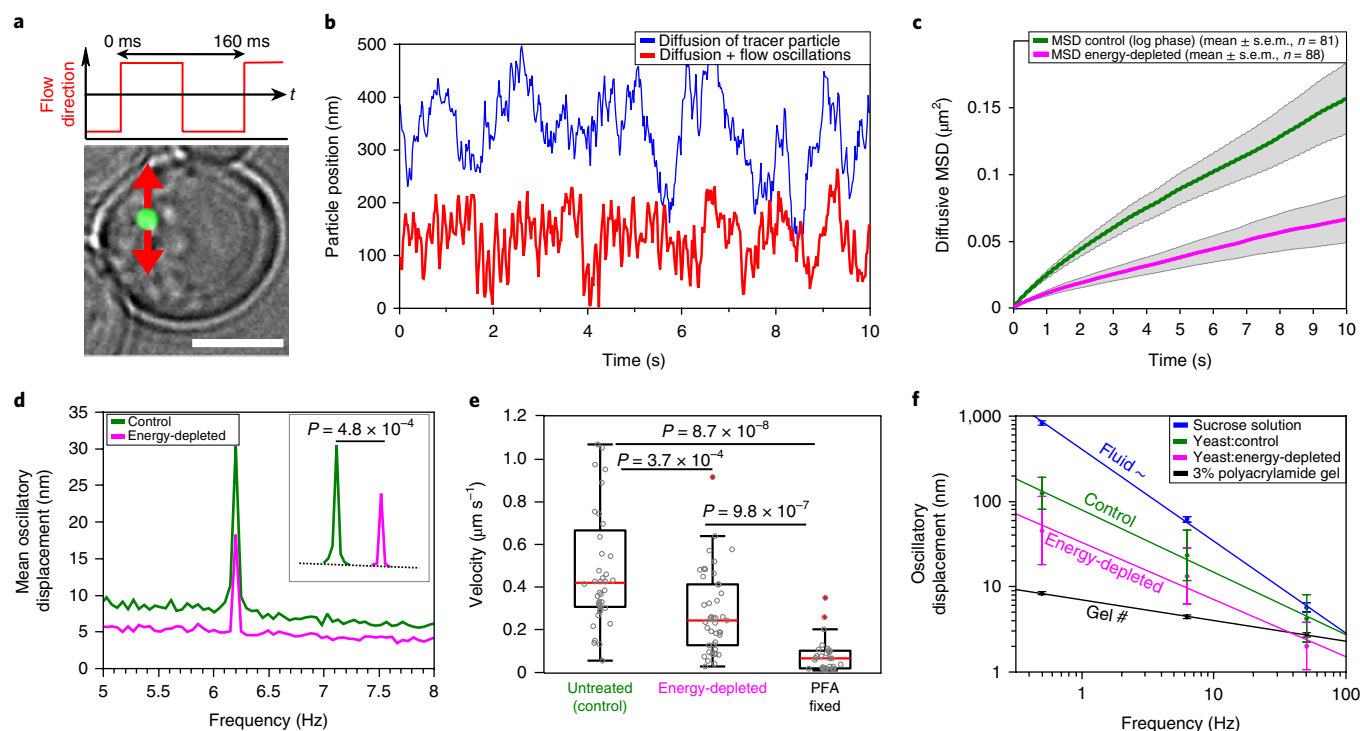
Fig. 6 | Intracellular flow perturbations reveal a fluid-to-solid transition in the cytoplasm of energy-depleted yeast cells. a, Genetically encoded fluorescent tracer particles (µNS, green) report on the amplitude of non-invasively induced cytoplasmic flows in yeast cells. Scale bar, 5 µm. A total of 81 biologically independent measurements were performed, with similar outcome. **b**, Example of a diffusive particle trajectory in the absence of flows (blue trace; 35 biologically independent measurements were performed with similar outcomes) and superimposed by weak oscillatory flows (red trace; 81 biologically independent measurements were performed with similar outcome. **c**, MSD curves show reduced diffusion in energy-depleted cells. Data represents mean ± s.e.m. with $n = 88$ and $n = 81$ single cell measurements for energy-depleted and control cells, respectively, pooled from 12 independent experiments for each condition. **d**, In agreement with the description of passive materials, reduced diffusion is in accordance with the reduction of inducible motion (reduction of mobility in both cases, within the range 0.5 ± 0.05). Inset, two-sample t-test. The data set in **d** is the same as the data set in **c. e**, Boxplot of oscillatory velocities for trajectories with a significant flow signal, analysed by two-sample t-test (same data set as for **c** and **d**). Cells have individually resolvable velocities. $n = 39$ for control, $n = 43$ for energy-depleted and $n = 26$ for PFA-fixed, where n represents single-cell measurements pooled from 12, 12 and 3 independent experiments, respectively. For each box, the red line indicates the median and the bottom and top edges of the box represent the 25th and 75th percentiles, respectively. The whiskers extend to the most extreme data points not considered outliers, and outliers are plotted as red symbols. **f**, Frequency-dependent flow amplitude, emphasizing a metabolically induced change in the passive material properties of the cytoplasm. With reference to the extreme cases of a pure fluid and a covalently crosslinked gel, our data explain the observed cytoplasmic arrest by the transition from a fluid to solid (non-flowing) cytoplasm. Data represent mean ± relative s.d. For yeast, each data point represents 28, 25 and 31 (control) and 28, 28 and 34 (energy-depleted) independent single-cell measurements obtained from nine independent experiments per data point, respectively. For fluid and gel experiments, each data point represents five independent measurements.

been debated whether metabolically triggered cytoplasmic arrest is due to (1) a reduction of ATP-dependent active processes that would keep the cytoplasm in a continuously re-organizing state or (2) a change in the passive material properties of the cytoplasm that results from a change in pH and/or crowding[19,20]. To test which biological scenario applies and whether the passive material properties of the cytoplasm change upon energy depletion, we used FLUCS for active and probe-free microrheology measurements inside fully intact *Saccharomyces cerevisiae* cells. For this, we complemented weak oscillatory flow stimuli throughout the yeast cytoplasm (Fig. 6a,b, Supplementary Fig. 6 and Supplementary Video 10) with high-resolution tracking of genetically encoded fluorescent particles (µNS)[6,19], which act as local reporters for cytoplasmic movement. To distinguish between induced oscillatory motion and overlaid diffusive motion (Fig. 6b), we used a frequency-domain lock-in technique. Consistent with previous reports[19], we found that the diffusive mobility of these particles in the yeast cytoplasm decreases upon energy depletion (Fig. 6c). At the same time, we found that these µNS particles could also be displaced by directed cytoplasmic flow perturbations (Fig. 6b, red trace). Accounting for 4.3×10^4

flow-driven particle paths in a total of 169 cells (81 control cells, 88 energy-depleted cells), we found average flow tracks of 22 ± 1.5 nm and 12 ± 0.9 nm for control and energy-depleted cells, respectively (Fig. 6d). On a single cell level, this corresponds to flow velocities of up to $1.1 \, \mu m \, s^{-1}$ for control and $0.6 \, \mu m \, s^{-1}$ for energy-depleted cells (Fig. 6e). Importantly, no flows were observed in paraformaldehyde-fixed cells, which practically excludes the possibility of whole-cell motion, and stress-response assays using Ded1-sfGFP, a sensitive marker for heat stress[30], remained negative much beyond the required temperature oscillation of $\Delta T = \pm 2 \, K$ (Supplementary Fig. 3e–i).

Energy-depletion stress induces solidification of the yeast cytoplasm. Comparing the observed diffusive and flow-induced dynamics of particles in the yeast cytoplasm, we found a relative starvation-induced mobility reduction by a near-identical factor of $\sim 0.5 \pm 0.05$ for both processes. This active microrheology experiment therefore directly shows the previously observed changes in intracellular mobility to be accompanied by material changes of the cytoplasm. We further found the reduced oscillatory mobility

upon energy depletion to apply for at least two orders of frequency (0.5–50 Hz, Fig. 6f). When compared to the extreme cases of a pure fluid and a covalently crosslinked non-flowing gel, we found that yeast cells position themselves in between. The absolute positioning is thus metabolically dependent, with energy-depleted cells being closer to a gel than control cells (note the log–log scale). Furthermore, a quantitative signature of slower velocities at low frequencies, which is especially true in the case of energy depletion, indicates that cytoplasmic fluidity reduces for motions greater than a few tens of nanometres (Supplementary Fig. 6e). Because the magnitude of induced thermoviscous flows is independent of the absolute viscosity of fluids[22] (Supplementary Video 1), we conclude that the arrested dynamics of the cytoplasm in energy-depleted yeast cells is most likely caused by an increase in long-range elastic interactions. Our active microrheology measurements using FLUCS directly confirm the model that the cytoplasm undergoes a metabolically dependent fluid-to-solid (non-flowing) transition upon energy depletion, as suggested for bacteria[6] and yeast[19,20]. Given the near-identical response from passive and active rheological measurements in yeast, we see little or no evidence for an energy-dependent active mobility (active diffusion) as it contributes to the cytoplasmic motion observed in larger, mammalian cells[7,18,31]. Compared to mammalian cells, unicellular organisms such as yeast neither have to contribute to a tightly controlled homeostatic environment nor can they rely on it. Such an autonomous lifestyle necessitates that yeast cells find other ways of adapting to stress. In the specific case of energy-depletion stress, this is achieved by entry into a state of cytoplasmic arrest.

Discussion

In summary, we have demonstrated the power of non-invasive intracellular flow perturbations—FLUCS. FLUCS perturbations are local, directed, dynamic, probe- and contract-free, physiological, and tractable by physical modelling of thermoviscous expansion phenomena.

As a new perturbation paradigm, FLUCS permits the dissection of the causal role of intracellular flows during the establishment and maintenance of polarity in *C. elegans* zygotes. In these early embryos, FLUCS enables precise active control of cytoplasmic motion, so that microscopy of developmental processes becomes interactive. Specifically, we found that cytoplasmic flows enhance the loading of PAR molecules to the zygote membrane. This suggests a functional role of comparably fast cytoplasmic flows during the wild-type polarization process, and more generally demonstrates that advective flows of the cytoplasm may strongly impact protein and possibly RNA localization in embryos. We therefore suggest FLUCS not only as a versatile tool to address the enigma of cytoplasmic streaming in a wide range of systems, but also to study the causes and consequences of protein localization in patterning systems, especially in early embryogenesis.

We have found that cytoplasmic flows efficiently couple to and thereby move the fluid actomyosin cortex during the maintenance phase. These experiments show that actomyosin flows[15,17] alone are sufficient to transport pre-established PAR domains over long distances, opening the door for a more detailed understanding of how PAR oligomerization states[32–34] impact cortical affinity. Downstream from PAR translocation, we have exemplified how flow-induced phenotypes can be used to study stability aspects of developmental programmes. Finally, we have shown how FLUCS enables active, probe-free rheology of the cytoplasm, allowing us to identify a fluid-to-solid transition as the mechanism underlying cytoplasmic arrest in energy-depleted yeast cells. Given the central role of intracellular transport processes in many proposed models of morphogenesis[1,2,10,35–41], cell motility[42], intracellular trafficking[43], directional segregation of phase-separated compartments during cell division[44], organization of the nucleus[45–47] and mimicry of active

biological fluids and gels[48–50], we conclude by emphasizing the enormous potential of FLUCS to probe how cells organize biochemical reactions into functional spatial structure.

Methods

Methods, including statements of data availability and any associated accession codes and references, are available at https://doi.org/10.1038/s41556-017-0032-9.

References

1. Turing, A. M. The chemical basis of morphogenesis. *Philos. T. R. Soc. Lond. B* **237**, 37–72 (1952).
2. Kondo, S. & Miura, T. Reaction–diffusion model as a framework for understanding biological pattern formation. *Science* **329**, 1616–1620 (2010).
3. Ganguly, S., Williams, L. S., Palacios, I. M. & Goldstein, R. E. Cytoplasmic streaming in Drosophila oocytes varies with kinesin activity and correlates with the microtubule cytoskeleton architecture. *Proc. Natl Acad. Sci. USA* **109**, 15109–15114 (2012).
4. Goldstein, R. E. & van de Meent, J.-W. A physical perspective on cytoplasmic streaming. *Interface Focus.* **5**, 20150030 (2015).
5. Howard, J., Grill, S. W. & Bois, J. S. Turing's next steps: the mechanochemical basis of morphogenesis. *Nat. Rev. Mol. Cell Biol* **12**, 400–406 (2011).
6. Parry, B. R. et al. The bacterial cytoplasm has glass-like properties and is fluidized by metabolic activity. *Cell* **156**, 183–194 (2014).
7. Guo, M. et al. Probing the stochastic, motor-driven properties of the cytoplasm using force spectrum microscopy. *Cell* **158**, 822–832 (2014).
8. Wolpert, L. Positional information and the spatial pattern of cellular differentiation. *J. Theor. Biol.* **25**, 1–47 (1969).
9. Schwartz, A. L. Cell biology of intracellular protein trafficking. *Annu. Rev. Immunol.* **8**, 195–229 (1990).
10. Gregor, T., Wieschaus, E. F., McGregor, A. P., Bialek, W. & Tank, D. W. Stability and nuclear dynamics of the bicoid morphogen gradient. *Cell* **130**, 141–152 (2007).
11. Brangwynne, C. P., Koenderink, G. H., Mackintosh, F. C. & Weitz, D. A. Cytoplasmic diffusion: molecular motors mix it up. *J. Cell Biol* **183**, 583–587 (2008).
12. Müller, P., Rogers, K. W., Yu, S. R., Brand, M. & Schier, A. F. Morphogen transport. *Development* **140**, 1621–1638 (2013).
13. Bray, D. & White, J. G. Cortical flow in animal cells. *Science* **239**, 883–888 (1988).
14. Mayer, M., Depken, M., Bois, J. S., Jülicher, F. & Grill, S. W. Anisotropies in cortical tension reveal the physical basis of polarizing cortical flows. *Nature* **467**, 617–621 (2010).
15. Munro, E., Nance, J. & Priess, J. R. Cortical flows powered by asymmetrical contraction transport PAR proteins to establish and maintain anterior-posterior polarity in the early C. elegans embryo. *Dev. Cell* **7**, 413–424 (2004).
16. Goldstein, B. & Macara, I. G. The PAR proteins: fundamental players in animal cell polarization. *Dev. Cell* **13**, 609–622 (2007).
17. Goehring, N. W. et al. Polarization of PAR proteins by advective triggering of a pattern-forming system. *Science* **334**, 1137–1141 (2011).
18. Riedel, C. et al. The heat released during catalytic turnover enhances the diffusion of an enzyme. *Nature* **517**, 227–230 (2015).
19. Munder, M. C. et al. A pH-driven transition of the cytoplasm from a fluid- to a solid-like state promotes entry into dormancy. *eLife* **5**, e09347 (2016).
20. Joyner, R. P. et al. A glucose-starvation response regulates the diffusion of macromolecules. *eLife* **5**, e09376 (2016).
21. Weinert, F., Kraus, J., Franosch, T. & Braun, D. Microscale fluid flow induced by thermoviscous expansion along a traveling wave. *Phys. Rev. Lett.* **100**, 164501 (2008).
22. Weinert, F. M. & Braun, D. Optically driven fluid flow along arbitrary microscale patterns using thermoviscous expansion. *J. Appl. Phys.* **104**, 104701 (2008).
23. Begasse, M. L., Leaver, M., Vazquez, F., Grill, S. W. & Hyman, A. A. Temperature dependence of cell division timing accounts for a shift in the thermal limits of C. elegans and C. briggsae. *Cell. Rep.* **10**, 647–653 (2015).
24. Vey, S. & Voigt, A. AMDiS: adaptive multidimensional simulations. *Comput. Vis. Sci.* **10**, 57–67 (2007).
25. Witkowski, T., Ling, S., Praetorius, S. & Voigt, A. Software concepts and numerical algorithms for a scalable adaptive parallel finite element method. *Adv. Comput. Math.* **41**, 1145–1177 (2015).
26. Hoege, C. & Hyman, A. A. Principles of PAR polarity in Caenorhabditis elegans embryos. *Nat. Rev. Mol. Cell Biol.* **14**, 315–322 (2013).
27. Motegi, F. et al. Microtubules induce self-organization of polarized PAR domains in Caenorhabditis elegans zygotes. *Nat. Cell Biol.* **13**, 1361–1367 (2011).

28. Hird, S. N. & White, J. G. Cortical and cytoplasmic flow polarity in early embryonic cells of Caenorhabditis elegans. *J. Cell Biol.* **121**, 1343–1355 (1993).

29. Schenk, C., Bringmann, H., Hyman, A. A. & Cowan, C. R. Cortical domain correction repositions the polarity boundary to match the cytokinesis furrow in *C. elegans* embryos. *Development* **137**, 1743–1753 (2010).

30. Wallace, E. W. J. et al. Reversible, specific, active aggregates of endogenous proteins assemble upon heat stress. *Cell* **162**, 1286–1298 (2015).

31. Hu, J. et al. Size- and speed-dependent mechanical behavior in living mammalian cytoplasm. *Proc. Natl Acad. Sci. USA* **114**, 9529–9534 (2017).

32. Dickinson, D. J., Schwager, F., Pintard, L., Gotta, M. & Goldstein, B. A single-cell biochemistry approach reveals PAR complex dynamics during cell polarization. *Dev. Cell* **42**, 416–434 (2017).

33. Rodriguez, J. et al. aPKC cycles between functionally distinct PAR protein assemblies to drive cell polarity. *Dev. Cell* **42**, 400–415 (2017).

34. Wang, S.-C. et al. Cortical forces and CDC-42 control clustering of PAR proteins for Caenorhabditis elegans embryonic polarization *Nat. Cell Biol.* **19**, 988–995 (2017).

35. Jaeger, J. et al. Dynamic control of positional information in the early *Drosophila* embryo. *Nature* **430**, 368–371 (2004).

36. Loose, M., Fischer-Friedrich, E., Ries, J., Kruse, K. & Schwille, P. Spatial regulators for bacterial cell division self-organize into surface waves in vitro. *Science* **320**, 789–792 (2008).

37. Hecht, I., Rappel, W.-J. & Levine, H. Determining the scale of the bicoid morphogen gradient. *Proc. Natl Acad. Sci. USA* **106**, 1710–1715 (2009).

38. Rulands, S., Klünder, B. & Frey, E. Stability of localized wave fronts in bistable systems. *Phys. Rev. Lett.* **110**, 038102 (2013).

39. He, B., Doubrovinski, K., Polyakov, O. & Wieschaus, E. Apical constriction drives tissue-scale hydrodynamic flow to mediate cell elongation. *Nature* **508**, 392–396 (2014).

40. Tayar, A. M., Karzbrun, E., Noireaux, V. & Bar-Ziv, R. H. Propagating gene expression fronts in a one-dimensional coupled system of artificial cells. *Nat. Phys.* **11**, 1037–1041 (2015).

41. Saha, S. et al. Polar positioning of phase-separated liquid compartments in cells regulated by an mRNA competition mechanism. *Cell* **166**, 1572–1584 (2016).

42. Svitkina, T. M. & Borisy, G. G. Arp2/3 complex and actin depolymerizing factor/cofilin in dendritic organization and treadmilling of actin filament array in lamellipodia. *J. Cell Biol.* **145**, 1009–1026 (1999).

43. Gilleron, J. et al. Image-based analysis of lipid nanoparticle-mediated siRNA delivery, intracellular trafficking and endosomal escape. *Nat. Biotechnol.* **31**, 638–646 (2013).

44. Brangwynne, C. P. et al. Germline P granules are liquid droplets that localize by controlled dissolution/condensation. *Science* **324**, 1729–1732 (2009).

45. Cremer, T. & Cremer, C. Chromosome territories, nuclear architecture and gene regulation in mammalian cells. *Nat. Rev. Genet.* **2**, 292–301 (2001).

46. Bolzer, A. et al. Three-dimensional maps of all chromosomes in human male fibroblast nuclei and prometaphase rosettes. *PLoS. Biol.* **3**, e157 (2005).

47. Solovei, I. et al. Nuclear architecture of rod photoreceptor cells adapts to vision in mammalian evolution. *Cell* **137**, 356–368 (2009).

48. Prost, J., Julicher, F. & Joanny, J.-F. Active gel physics. *Nat. Phys.* **11**, 111–117 (2015).

49. Faubel, R., Westendorf, C., Bodenschatz, E. & Eichele, G. Cilia-based flow network in the brain ventricles. *Science* **353**, 176–178 (2016).

50. Needleman, D. & Dogic, Z. Active matter at the interface between materials science and cell biology. *Nat. Rev. Mater.* **2**, 17048 (2017).

Author contributions

M.Mi., A.W.F. and M.Kr. designed the experimental set-up. M.Mi. conducted experiments. M.Mi. and M.Kr. analysed data. M.Mi. wrote the initial draft. P.G. assisted with *C. elegans* experiments and provided worm lines. M.N. and A.V. performed finite-element simulations. C.I. and M.Mu. helped with yeast measurements. M.Ka. assisted with gel chemistry. M.Mi., P.G., A.W.F., S.W.G. and M.Kr. conceived and interpreted *C. elegans* experiments, M.Mi., S.A. and M.Kr. conceived and interpreted yeast experiments. All authors contributed to a critical discussion of the data and participated in writing the manuscript, which M.Mi. and M.Kr. finalized. M.Kr. coordinated the research.

Competing interests

The authors declare that parts of the published work led to the application for a European patent.

Additional information

Supplementary information accompanies this paper at https://doi.org/10.1038/s41556-017-0032-9.

Reprints and permissions information is available at www.nature.com/reprints.

Correspondence and requests for materials should be addressed to M.K.

Publisher's note: Springer Nature remains neutral with regard to jurisdictional claims in published maps and institutional affiliations.

Methods

FLUCS. *Optical setup.* To carry out physical transport perturbations inside cells and developing embryos, an infrared custom-coated objective lens was used (×60 UPLSAPO, NA = 1.2, W-IR coating, Olympus), operated with heavy water (D$_2$O) immersion between the lens and coverslip to ensure compatibility with 1,455 nm laser light. Imaging and manipulations were carried out on an open but mechanically robust microscope platform (RM21, Mad City Labs) equipped with a piezo stage (Nano-Drive 3, Mad City Labs). See Supplementary Fig. 1a,b for details of the set-up. Bright-field (BF) illumination was achieved through a second, custom-built microscope in upright geometry, which was also used for rapid sample localization. BF and fluorescent imaging were performed using an sCMOS camera (Zyla 5.5, Andor). Of note, differential interference contrast (DIC) imaging was compromised due to constraints on the thermal design of the imaging chamber (see next paragraph), which necessitated the use of high thermally conductive birefringent sapphire crystals.

For submillisecond thermal manipulations, an infrared laser beam was acoustically scanned through the sample. In detail, a fibre-based infrared Raman laser (CRFL-20-1455-OM1, 20 W, near TEM00 mode profile, Keopsys) in continuous-wave (c.w.) mode at a wavelength of 1,455 nm, was linearly polarized (CCM1-PBS254/M, Thorlabs) and expanded to match the aperture of the acousto-optical deflector (AOD, ATM-802FA49, IntraAction). Precise deflection patterns were generated using a dual-channel frequency generator PCI card (DVE 120, IntraAction), controlled via modified LabVIEW (National Instruments) based control software (DVE 120 control, IntraAction), in combination with a power amplifier (DPA-504D, IntraAction). For two-dimensional laser scans (Fig. 4a), a two-axis acousto-optical deflector (AA.DTSXY-A6-145, Pegasus Optik) was used. Precise laser scan patterns were performed by generating analog signals using self-written software in LabVIEW, in combination with a PCI express card (PCIe 6369, National Instruments). This analog signal was high-frequency-modulated using an electronic oscillator (AA.DRFAI0Y-B-0-x, Pegasus Optik) to match the frequency domain of the crystal inside the deflector. The high-frequency signal was further amplified using an electronic amplifier (2.5 W, AA.AMPA-B-34-20.4, Pegasus Optik).

The plane of laser deflection was imaged into the back focal plane (BFP) of the objective lens via a magnifying 4–f telescope (lenses AC254-C series, Thorlabs). Focal plane agreement for visible and infrared wavelengths was confirmed using knife-edge-type[51] scanning of a chromium mask through the laser focus, combined with integrating sphere detection (S146C, Thorlabs). The imaging path and laser beam were combined by a dichroic mirror (DM2: DMSP805, Thorlabs). For fluorescent imaging, green fluorescent protein (GFP; MDF-GFP, Thorlabs), tetramethylrhodamine (MDF-TRITC, Thorlabs) and Texas Red (MDF-TXRED, Thorlabs) filter sets were combined with sub-millisecond controlled light-emitting diodes (LEDs; M470L3, M565L3 LEDs in combination with LED driver LDC240C, Thorlabs).

Heat management and mounting of embryos. To efficiently remove excess heat from the samples (for example, the *C. elegans* embryos), thin mounting chambers were constructed based on a standard coverslip (18 × 18 × 0.17 mm³; Menzel) facing the objective lens and a high thermal conductive sapphire cover slide (thermal conductivity of 27.1 W m^{-1} K^{-1}, SMS-7521, UQG Optics) closing the sandwich-like chamber from the top. During flow manipulation experiments inside the *C. elegans* embryos, the microscope stage was actively cooled from an ambient temperature of 18 °C to 15 °C using proportional–integral–derivative (PID) controlled Peltier elements (TES1-127021, TEC, Conrad). In this way we made sure that the maximum deviation from the ambient temperature equaled half the laser-induced temperature increase. Temperature decreases must therefore be understood as reductions of the ambient temperature. These were directly attached to the 1.0-mm-thick sapphire cover slide, resulting in a thermal response time of ~1 s.

The height of the buffer-filled chamber was controlled using polystyrene beads with a diameter of 5–25 μm (Polybead, Polysciences) and a typical volume fraction of 0.05% as spacers. The resulting chamber height was verified by visual determination of the chamber limiting surfaces using a piezo stage.

Time-resolved fluorescence–temperature measurements. To experimentally determine the submillisecond dynamic temperature distribution during flow perturbation experiments, temperature profiles resulting from scanning the infrared laser beam were imaged stroboscopically using a temperature-sensitive fluorescent dye, Rhodamine B (Sigma-Aldrich). As described previously[22], the temperature-dependent relative quantum efficiency of the dye was first determined by bulk measurement (Supplementary Fig. 1c), revealing a temperature-dependent decrease 1.2% K^{-1} at room temperature. The fluorescence intensity was then used to infer dynamic temperature changes within a stroboscopically reconstructed temperature cycle. Because diffusion is ~1,000 times faster for heat than for the Rhodamine B dye, time-invariant thermophoretic contributions[52] to the signal (accounting for about 20% of the initial signal change) can be separated.

Supplementary Fig. 1d shows a kymograph of the dynamic temperature distribution in a 15-μm-thick chamber with a period of 0.5 ms, with thermal relaxation times of ~110 μs (Supplementary Fig. 1e and Supplementary Video 4). Negative differential temperatures account for stage cooling below ambient room

temperature, as was used for actual experiments within cells and embryos. Time-average temperature profiles were calculated either based on a longer exposure time, or from the mean fluorescence reduction during one stroboscopically reconstructed temperature cycle.

Infrared absorption inside embryos and cell extracts. To infer the temperature distribution inside the *C. elegans* embryo, explicit measurements of laser beam transmission through individual embryos (1–16 cell stage) were performed. An integrating sphere was mounted directly on top of the upper coverslip to measure the infrared laser power passing the embryo or the water layer next to the embryo (reference) (Supplementary Fig. 2a). Measurements were performed in a 30-μm-thick chamber using a ×40 air objective (UPLSAPO ×40, NA = 0.95, Olympus). Using a piezo-stage the static laser spot was repeatedly transmitted through the embryo and next to the embryo through the mounting buffer. This relative transmission determination was repeated ten times per embryo, and the average transmission was computed for a single embryo. In total, 13 embryos were analysed, and a slight decrease of 1.8 ± 0.9% (mean ± s.d., n = 13) in the relative transmission compared to water (9.5% absorption) was observed (Supplementary Fig. 2b). Although these integrating-sphere-based measurements of forward transmitted light cannot distinguish between beam attenuation due to scattering or absorption, they allow us to determine a precise upper bound of absorption of the *C. elegans* cytoplasm of 1.19 relative to that of water. Because of the strong scattering of light by micrometre-scale yolk granules, even this slightly increased absorption coefficient in the cytoplasm must be seen as a conservative overestimate of the actual heat-inducing absorption.

The view that *C. elegans* embryos and other cells do not absorb more light at 1,455 nm than water receives further support from bulk measurements of laser light transmission at this wavelength through ~130-μm-thick chambers filled with water, 10% aqueous BSA solution, egg extract from *X. laevis* and the ultracentrifuged lipid fraction of yolk from an unfertilized chicken egg (Supplementary Fig. 2c). We found that, relative to the measurement of water (penetration depth of 305 μm), the transmission increased by 4, 3 and 14% for BSA, cell extract and yolk, respectively (Supplementary Fig. 2d). Reflection changes due to an increasing refractive index can maximally account for 0.7% of this signal change, as calculated according to the Fresnel equations. Therefore, the absorption properties of the *C. elegans* embryo are mainly determined by the absorption of water and are probably even slightly lower.

X. laevis extract from unfertilized frog eggs was prepared as published[53], including protease inhibitors (leupeptin, pepstatin and chymostatin) and cytochalasin D to a final concentration of 10 μg ml^{-1} each.

A step-by-step protocol describing how to apply FLUCS in single cells and developing embryos can be found at the Nature Protocol Exchange[54].

C. elegans strains and growth conditions. *C. elegans* line TH120[55] was used, with PAR-2 labelled with GFP and PAR-6 labelled with mCherry (all TH lines were provided by the Hyman lab). Line TH306 with non-muscle myosin 2 was labelled with GFP and PAR-2 labelled with mCherry. Line SWG007[56] with non-muscle myosin 2 labelled with GFP and lifeAct labelled with mKate2. Line LP675[32] with PAR-2 was labelled with mNeonGreen and PAR-6 with mKate2. The *C. elegans* stocks were maintained at ~19 °C and cultured as described in ref. [57]. Embryos were dissected in a 4–6 μl drop of M9 buffer and mounted on the custom-built temperature stage using polystyrene beads as spacers. All animals were handled according to Directive 2010/63/EU on the protection of animals used for scientific purposes and German animal welfare law under the licence document no. DD24-5131/367/9 from Landesdirektion Sachsen (Dresden) Section 24D.

Yeast cultivation and starvation conditions. *S. cerevisiae* were grown at 25 °C in yeast synthetic complete medium (S-complete) or synthetic dropout (SD) medium. The SD medium had a pH of ~5.5. *S. cerevisiae* cells were energy-depleted by incubation in SD medium, without glucose, containing 20 mM 2-deoxyglucose (2-DG, inhibition of glycolysis) and 10 mM antimycin A (inhibition of mitochondrial ATP production) for 2 h before flow induction. This treatment causes a more than 95% reduction in cellular ATP[58]. To tightly adhere the cells to the coverslip, a thin layer of lectin from *Bandeiraea simplicifolia* (L2380, Sigma Aldrich) or concanavalin A from *Canavalia ensiformis* (C7275-250MG, Sigma Aldrich) was transferred to the coverslip surface.

The following *S. cerevisiae* strains were used in the study. For heat shock experiments we used W303 ADE+Ded1-sfGFP(V206K) and Pab1-mCherry with the genetic background *W303 MATα can1-100 his3-11,15 leu2-3,112 trp1-1 ura3-1 Ded1-sfGFP-KanMX Pab1-mCherry-HygB*. For microrheology experiments we used W303 ADE+pAG415GPD-EGFP-μNS[19] with the genetic background *303 MATα can1-100 his3-11,15 leu2-3,112 trp1-1 ura3-1 pAG415GPD-EGFP-μNS*.

Viability tests of C. elegans embryos in response to laser-induced heating. The body temperature of nematodes such as *C. elegans* depends on the ambient temperature, and the early embryonic development in particular has a well-characterized response to temperature changes[23]. Their entire life-cycle is compatible with temperatures from 11 to 26 °C. In dedicated viability experiments, embryos at different developmental stages were heated statically for at least 30 s with a

highly focused laser beam at 10 mW (Supplementary Fig. 3a). The temperature distribution within the embryo was simulated using the finite-element software COMSOL, leading to a peak temperature of ~32 °C, which is in good agreement with an analytical solution commonly used to calculate laser-induced heating in optical traps[59]. After this heating, normal cell divisions were observed (Supplementary Fig. 3b). As one would expect, damage to the developing embryos was observed as a consequence of localized heating above 44 °C for 30 s (data not shown).

To mimic the dynamic temperature fields typically used to induce flows, we applied a laser scan at a repetition rate of 10 kHz with a triangular wave mode at 60 mW to avoid flows (Supplementary Fig. 3c and Supplementary Video 5). In this way, only a temperature field was induced, and no flows were created. We heated the embryos from room temperature (here 20 °C) to 32 °C. No developmental abnormalities after multiple rounds of cell division were observed (Supplementary Fig. 3d). It is noteworthy that the temperature required to induce significant flow velocities in the *C. elegans* embryo lies a factor of three below the temperatures applied here for survival experiments (no developmental alterations detected). The observed robustness of the developing *C. elegans* embryo to short and localized temperature is in agreement with previous literature reports.

Heat shock of S. cerevisiae in response to global heating and laser-induced heating. To further validate the response of laser-induced heating on cellular homeostasis, we used the well-characterized model organism *S. cerevisiae*. The induction of heat shocks in single cells and its readout through fluorescent heat shock proteins emerged as a robust test for the stress response. Even more sensitive to mild and short temperature changes are stress granule proteins such as Ded1, which form aggregates within minutes[30]. Here, we used the protein Ded1-sfGFP as a marker for the temperature-induced stress response.

We first characterized the formation of stress granules in response to a global temperature increase. We mounted the *S. cerevisiae* cells on a highly conductive sapphire slide connected to PID-controlled Peltier elements, enabling rapid and precise temperature control. At global temperatures of ~43 °C, significant formation of stress granules was observed (Supplementary Fig. 3e–h). Next, we performed laser-induced heating by scanning at a repetition rate of 2 kHz over the cells, as for the microrheology experiments (Supplementary Fig. 3i). Only at unnecessarily high laser powers (corresponding to about three times higher temperatures than used for the microrheology experiments) were stress granules formed. This experiment shows that the laser-induced temperature does not generate additional stress responses under standard microrheology conditions.

Particle image velocimetry (PIV). Flow fields were visualized by tracer particles. These were either fluorescent microspheres (FS03F, Bang labs, Polysciences), fluorescent viral matrix particles (see section 'Single-particle localization and Fourier detection of oscillatory flows' for details in the Methods) or, in the case of *C. elegans*, optically resolvable lipid yolk granules, imaged with a high NA of 1.2. Flow fields were analysed using PIVlab[60], a digital PIV tool for MATLAB, to quantitatively determine velocity flow fields in vitro as well within living cells and developing embryos. The software calculated the velocity distribution within image pairs using a direct Fourier transform correlation with multiple passes and deforming windows. Specifically, flow fields were computed with two passes, with $40 \times 40\,px^2$ and a $20 \times 20\,px^2$ sample areas, respectively. Flow fields were computed by averaging consecutive frames over 20 s, individual static trajectories likely resulting from cytoskeleton-anchored objects were manually removed. Additionally, the magnitude of flow velocities was compared to trajectories measured with the segmented line-tool in FIJI[61], and found to be consistent with the PIV results.

Quantification of flow velocities induced in the cell extract. Flows were generally induced by unidirectional, repeated scanning of an infrared laser beam through a given liquid solution, visualized with the aid of fluorescent tracer microspheres and automatically tracked using the Mosaic single-particle tracker[62]. Flow profiles were determined in water, water–glycerol (50% vol/vol) and pure honey for calibration and illustration purposes. Flow velocities in *X. laevis* cell extracts were quantified for varying temperature increases at a scanning frequency of 2 kHz, which is compatible with temperature oscillations on cellular length scales (Supplementary Fig. 4a). The results were successfully fitted with a previously described quadratic equation for viscous non-biological media[22] (Supplementary Fig. 4b).

Quality control of intracellular flow perturbation experiments. To obtain robust and reproducible data, we verified the calibration of the FLUCS set-up at the beginning of each experimental day. This was done by measuring the flow profile and velocity in our standard calibration slide, as shown in Fig. 1c. Embryos and cells were maintained as described in the extended protocol, found at the Nature Protocol Exchange[54]. Once an experimental procedure was established, flow experiments were performed inside *C. elegans* embryos and yeast cells under near-identical experimental conditions (laser parameters, chamber height, sample condition).

Image analysis of PAR-2 perturbation measurements. For kymographic analysis (including centre-of-mass motion), raw images were corrected by subtraction of a

dark frame. Bleaching of GFP (~25% over the length of the movies) was corrected by embryo-wide normalization of the fluorescent signal.

Kymographs of the temporal evolution of the GFP-PAR-2 domain in response to flows applied perpendicular (Fig. 3) or parallel (Fig. 4) were generated by manually tracking the PAR-2 domain then using the FIJI built-in function 'straighten' to unwrap the curved signal. The final kymograph was computed from a maximum signal projection in the radial direction, providing high-quality positional and temporal information about the membrane signal. Data presented in Fig. 3a,c and Fig. 4b,c are based on five consecutive frames by averaging the data over 1.6 s in total, to increase the signal-to-noise ratio for display purposes.

The average translocation velocity of the PAR-2 domain was determined by dividing the centre-of-mass position by the frame duration (i.e. velocity $v = dx/dt$). The coupling efficiency η_c between induced membrane-near flows and the resulting translocation of the PAR-domain was estimated as the ratio of the average velocity of the PAR domain v_d and membrane-near flows v_i:

$$\eta_c = \frac{v_d}{v_f}, \text{with} \quad \langle \eta_c \rangle = 0.51 \pm 0.14 \quad (\text{mean} \pm \text{s.d}, n = 6) \tag{1}$$

Consideration of induced advective flow transport in the cytosol. To define the relative contribution of advective compared to diffusive transport of a molecule, the dimensionless Péclet number (Pe) was used: if Pe > 1, advection dominates. Specifically, Pe is given as the ratio of the time to travel a characteristic length L by diffusion with a diffusion coefficient D, compared to the time to travel L by advective transport at a given flow velocity v, in our case by induced hydrodynamic flows:

$$Pe = \frac{v \cdot L}{D} \tag{2}$$

By using measured values of the PAR-2 protein diffusion constant in the *C. elegans* embryonic cytosol ($D \approx 1.5\,\mu m^2\,s^{-1}$) (ref. [63]), together with an induced velocity of $v \approx 15\,\mu m\,min^{-1}$ over a distance $L \approx 30\,\mu m$, we obtain Pe ≈ 5. Hence, advective flow-driven transport dominates over diffusive fluxes inside the cytosol.

Physical modelling of flows inside the C. elegans embryo with extension of existing simulations. To compute the velocity $\mathbf{u}$ and the pressure p for hydrodynamic flows induced by dynamic temperature fields inside the *C. elegans* embryo (that is, by scanning an infrared laser beam), we solved the Stokes equation by finite element (FEM) simulations, using the toolbox AMDiS[24,25]. Straightforward calculus and factoring all constants into pressure yields the following system of momentum balance (equation (3)) and mass continuity (equation (4)):

$$-\nabla((1-\beta\Delta T)(\nabla\mathbf{u} + \nabla\mathbf{u}^T)) + \nabla\tilde{p} = 0 \tag{3}$$

$$(1-\alpha\Delta T)\nabla\cdot\mathbf{u} - \alpha\nabla\Delta T\cdot\mathbf{u} = \alpha\partial_t(\Delta T) \tag{4}$$

This means we have treated the cytoplasm as a Newtonian liquid that changes density only with changing temperature, not pressure[21]. Specifically, the effects of thermoviscous expansion were modelled by the linear relation between the temperature change ΔT and density $\rho = \rho_0(1-\alpha\Delta T)$ and viscosity $\eta = \eta_0(1-\beta\Delta T)$ [21].

In contrast to previously presented simulations of flows induced around a continuously moving, time-invariant heat spot[22], the here presented simulations also take into account temporal changes of the temperature field, as they are essential to describe flows induced over finite distances and to account for source terms emerging from an intensity modulation of a laser along its trajectory. To account for mass balance in finite geometries, we used impermeable boundaries with either no-slip (default for all simulations of induced flows) or constant tangential velocity boundary conditions (to simulate the cortical flows in Fig. 4e).

Source term modelling. Extending previous simulations[22], which assumed a constant temperature modulation $A(t) = $ const., we modelled the rapidly oscillating temperature fields via a constant temperature profile $\mathbb{X}(\mathbf{x})$, combined with a time-varying amplitude $A(t)$. For the trajectory of this configuration we assumed a periodic and unaccelerated movement with u_s. With such modelling, we obtained an additional source term f_a:

$$\Delta T(\mathbf{x},t) = A(t)\mathbb{X}(\mathbf{x}-\mathbf{u}_s t) \tag{5}$$

$$\alpha\partial_t(\Delta T)(\mathbf{x},t) = \alpha\partial_t A(t)\mathbb{X}(\mathbf{x}-\mathbf{u}_s t) - \alpha A(t)\nabla\mathbb{X}(\mathbf{x}-\mathbf{u}_s t)\cdot\mathbf{u}_s \tag{6}$$

$$f = f_a + f_b \tag{7}$$

To determine the implications of this modelling we used linearity (w.r.t. source terms f_a and f_b) of equation (6)) to investigate the impact of these source terms separately. As shown in Supplementary Fig. 5a, both source terms yield mean flows $\bar{u}_a$, $\bar{u}_b$ of compressible flow type with a distinct source–sink configuration ($\bar{u}_b$ reproduces the simulation results in ref. [22]). Further simulations yielded a net

flow oriented for $\tilde{u}_a$ in the direction of the laser movement, while $\tilde{u}_b$ generated a net flow with opposite direction. Only the combination of both source term effects (with thermoviscous expansion $\beta > 0$; see Supplementary Fig. 5b) reproduced the experimentally observed fluid flows, which are predominately incompressible type. Of note, temporally variant terms are equally essential to account for intensity changes along the laser path (and implicit to all modelling of experiments).

Numerical simulation of three-dimensional temperature profile. The shape of the volumetric temperature profile around a heating laser beam was calculated with the commercially available finite-element software COMSOL 5.1 (Supplementary Fig. 3d,e). The waist of the Gaussian beam was determined using the knife-edge[51] scanning technique, implemented by translating a binary chromium mask within the focal plane (Supplementary Fig. 3f), with a standard deviation of $c = 1.89\,\mu m$ for the fitted error function. The laser beam acted as a three-dimensional heat source, modelled as a focused Gaussian beam:

$$I(r,z) = I_0 \left(\frac{w_0}{w(z)}\right)^2 \exp\left[-\frac{2r^2}{w(z)^2}\right], \qquad (8)$$

where I_0 is the peak intensity at the centre of the beam, r is the radius, $w(z) = w_0\sqrt{1 + (z/z_0)^2}$ is the waist of the beam, $w_0 = 2c$ and $z_0 = \pi w_0^2/\lambda$ is the Rayleigh range. In agreement with this simulation result, laser-induced heating was further implemented as a radially Gaussian temperature distribution with quadratic modulation along the optical axis. Reduced efficiency of the laser deflector for high angles was taken into account by a centre-symmetric sinusoidal modulation $A(t) = \Delta T_m \sin^2(\pi/T)$, of the moving heat source along the 30-μm-long scanning path, with ΔT_m being the maximal temperature amplitude.

Explicit simulations of flows in C. elegans embryos. For numerical experiments, we approximated the geometry of the one-cell embryo as an ellipsoidal shape (semi-principal axes: 25 μm, 15 μm and 10 μm) and assumed a water-like cytoplasm with a thermal expansion coefficient of $\alpha = 3.3 \times 10^{-4}\,K^{-1}$ and temperature-dependent viscosity coefficient $\beta = 0.021\,K^{-1}$. We considered a heat spot with a full-width at half-maximum of 9.5 μm and a maximal temperature amplitude of $\Delta T_m = 6\,K$ (Supplementary Fig. 5c), which moved along a straight line of length $L = 30\,\mu$m in 0.5 ms. This width of the heat spot is also in good agreement with stroboscopic measurements. From the instantaneous flow field of a full cycle along the x axis, we computed the mean flow, as shown in Supplementary Fig. 5d. The mean flow consisted of two barrel-like vortices alongside the trajectory of the heat spot. Characteristically, the vortices rotate contrary to the direction of movement of the heat spot.

Coupling of cytoplasmic and cortical flows. To complement the experimental findings shown in Fig. 4, where externally induced hydrodynamic flows parallel to the cell cortex lead to significant translocation of the membrane-bound PAR-2 proteins, we performed three-dimensional FEM simulations in an embryonic-like geometry. To decipher whether the induced cytoplasmic flows are capable of coupling to and thereby inducing flows in cortical regions, we first investigated the impact of the geometry-dependent boundary effects on temperature-induced mean flow. We thus performed simulations with different distances between the induced flow and the boundary (Supplementary Fig. 5e). In particular, we observed, for a reduced distance, a continuous compression of the vortex trapped between the boundary and flow centre, which transitioned to a single vortex configuration for a distance smaller than 5 μm. This means that flows induced in proximity to the membrane maintain their directionality in the cortical region and are even faster than the flow induced inside the cytoplasm (Supplementary Fig. 5f). Furthermore, we computationally reconstructed the wild-type scenario where cortical flows close to the membrane of the embryo induce cytoplasmic flows (Supplementary Fig. 5g). For this, we simulated the cytoplasm with a prescribed tangential velocity at the cortex having a rotational symmetry with regard to the AP axis of the cell (Supplementary Fig. 5h). In these simulations, we observed that cortical flows induced cytoplasmic flows (Supplementary Fig. 5i) reaching up to 30% of the distance from the cortex to the AP axis into the cytoplasm (Supplementary Fig. 5j).

Together, this suggests that cytoplasmic flows induced in parallel to the cortex couple very efficiently to flows in the cortical region, thereby transporting PAR proteins along the membrane. Throughout the performed simulations we were able to qualitatively and quantitatively reproduce the observed flows presented in Fig. 1d and Fig. 4a.

Single-particle localization and Fourier detection of oscillatory flows. To induce oscillatory hydrodynamic flows in yeast cells, we applied flows in alternating, opposing directions for half periods of 80 ms, before reversing the flow (160 ms for a full period). Flow induction was performed with temperature variations of $\pm 2\,K$ and a base frequency of 2 kHz. These oscillatory flows were tracked by the motion of genetically encoded fluorescent viral matrix proteins (μNS)[6,19]. Using an exposure time of 15 ms and a frame rate of 50 Hz, these brightly fluorescent particles were localized with an accuracy of ± 2.6 nm (Supplementary Fig. 6a) at

typical drift velocities of the stage of <1 nm s^{-1} (Supplementary Fig. 6b), using the Mosaic single-particle tracker[62]. Mean squared displacement (MSD) analysis was performed as described previously[19], using the MATLAB script MSDanalyzer[64].

Flow velocities in the presence of particle diffusion were obtained by particle tracking in 1,024-frame movies and subsequent fast Fourier transform of the particle trajectories to obtain the power spectral density (PSD). Accurate synchronization of the laser-driven flow and the imaging camera ensured that the magnitudes of oscillatory flows were visible as a single sharp peak at the correct frequency (Supplementary Fig. 6c). The uncertainty of this signal was determined as the variance of the underlying noise floor.

To determine the physical state of the cytoplasm of *S. cerevisiae* under normal conditions as well as during starvation (energy-depleted), we induced hydrodynamic oscillations at a frequency of 6.25 Hz to perform active probe-free rheology for 20.48 s per cell. This choice combines good statistics for flow-driven oscillations on the single-cell level (125 full periods per cell) with the ability to quickly measure many cells.

Statistics and reproducibility. All statistical tests were performed in Matlab 2015b. The results in Fig. 1c,e, Fig. 3e, Supplementary Fig. 2b,d,f, Supplementary Fig. 4b and Supplementary Fig. 6b,c represent mean ± s.d. Results in Fig. 6c represent mean ± s.e.m. Results in Fig. 6e are presented as a box plot overlaid with individual data points (see dedicated caption for details). Results in Fig. 6f and Supplementary Fig. 6d,e represent mean ± relative s.d. To calculate P values, a two-tailed t-test was performed. All experiments without or with quantification were independently repeated at least three times with similar results, and representative data are shown. Exact sample numbers (that is, biologically independent repeats) and how often phenotypical outcomes were observed are indicated in the corresponding figure or figure legend.

Life Sciences Reporting Summary. Further information on experimental design is available in the Life Sciences Reporting Summary.

Code availability. Computational code for FEM simulations performed using AMDIS, self-written Matlab codes to perform Fourier analysis of single-cell oscillation experiments, and code for hardware control written in LabVIEW are available from the corresponding author upon request.

Data availability. All data supporting the findings of this study are available from the corresponding author upon reasonable request. This includes raw data such as unprocessed microscopy movie files and independent replicates, which are not directly displayed in the manuscript, although included in the data analysis in the form of graphs.

References

51. de Araújo, M. A. C., Silva, R., de Lima, E., Pereira, D. P. & de Oliveira, P. C. Measurement of Gaussian laser beam radius using the knife-edge technique: improvement on data analysis. *Appl. Opt.* **48**, 393–396 (2009).
52. Duhr, S. & Braun, D. Why molecules move along a temperature gradient. *Proc. Natl Acad. Sci. USA* **103**, 19678–19682 (2006).
53. Hannak, E. & Heald, R. Investigating mitotic spindle assembly and function in vitro using *Xenopus laevis* egg extracts. *Nat. Protoc.* **1**, 2305–2314 (2006).
54. Mittasch, M. et al. How to apply FLUCS in single cells and living embryos. *Nat. Protoc. Exch.* https://doi.org/10.1038/protex.2017.157 (2017).
55. Schonegg, S., Constantinescu, A. T. & Hoege, C. & Hyman, A. A. The Rho GTPase-activating proteins RGA-3 and RGA-4 are required to set the initial size of PAR domains in Caenorhabditis elegans one-cell embryos. *Proc. Natl Acad. Sci. USA* **104**, 14976–14981 (2007).
56. Reymann, A.-C., Staniscia, F., Erzberger, A., Salbreux, G. & Grill, S. W. Cortical flow aligns actin filaments to form a furrow. *eLife* **5**, e17807 (2016).
57. Brenner, S. The genetics of *Caenorhabditis elegans*. *Genetics* **77**, 71–94 (1974).
58. Serrano, R. Energy requirements for maltose transport in yeast. *Eur. J. Biochem.* **80**, 97–102 (1977).
59. Peterman, E. J. G., Gittes, F. & Schmidt, C. F. Laser-induced heating in optical traps. *Biophys. J.* **84**, 1308–1316 (2003).
60. Thielicke, W. & Stamhuis, E. J. PIVlab—towards user-friendly, affordable and accurate digital particle image velocimetry in MATLAB. *J. Open Res. Softw.* **2**, 1202–1210 (2014).
61. Schindelin, J. et al. Fiji: an open-source platform for biological-image analysis. *Nat. Methods* **9**, 676–682 (2012).
62. Sbalzarini, I. F. & Koumoutsakos, P. Feature point tracking and trajectory analysis for video imaging in cell biology. *J. Struct. Biol.* **151**, 182–195 (2005).
63. Petrásek, Z. et al. Characterization of protein dynamics in asymmetric cell division by scanning fluorescence correlation spectroscopy. *Biophys. J.* **95**, 5476–5486 (2008).
64. Tarantino, N. TNF and IL-1 exhibit distinct ubiquitin requirements for inducing NEMO–IKK supramolecular structures. *J. Cell Biol.* **204**, 231–245 (2014).

natureresearch

Corresponding author(s): Moritz Kreysing

☐ Initial submission ☐ Revised version ☒ Final submission

Life Sciences Reporting Summary

Nature Research wishes to improve the reproducibility of the work that we publish. This form is intended for publication with all accepted life science papers and provides structure for consistency and transparency in reporting. Every life science submission will use this form; some list items might not apply to an individual manuscript, but all fields must be completed for clarity.

For further information on the points included in this form, see Reporting Life Sciences Research. For further information on Nature Research policies, including our data availability policy, see Authors & Referees and the Editorial Policy Checklist.

▶ Experimental design

1. Sample size

Describe how sample size was determined.

We performed no statistical test to predetermine the sample size. The sample size was determined by counting single cells and embryos under the microscope.

2. Data exclusions

Describe any data exclusions.

No animals, cells or data were excluded from statistics

3. Replication

Describe whether the experimental findings were reliably reproduced.

For all experiments presented in this study, at least three biologically independent measurements were performed showing a similar outcome and the representative data are shown. Each Experiments was performed by applying the same technical protocol as identified in initial test experiments. The number of replications is represented in each figure panel or in the respective caption.

4. Randomization

Describe how samples/organisms/participants were allocated into experimental groups.

No randomization was used to allocate sample size, since the animals or cells did not exhibit any significant differences.

5. Blinding

Describe whether the investigators were blinded to group allocation during data collection and/or analysis.

For C. elegans, embryos were only selected for the correct developmental stage and not disregard because of some other features. For yeast single measurements, cells were selected randomly to reduce bias. Investigators were not blinded during the computer based data analysis.

Note: all studies involving animals and/or human research participants must disclose whether blinding and randomization were used.

6. Statistical parameters

For all figures and tables that use statistical methods, confirm that the following items are present in relevant figure legends (or in the Methods section if additional space is needed).

n/a	Confirmed	
☐	☒	The exact sample size (*n*) for each experimental group/condition, given as a discrete number and unit of measurement (animals, litters, cultures, etc.)
☐	☒	A description of how samples were collected, noting whether measurements were taken from distinct samples or whether the same sample was measured repeatedly
☐	☒	A statement indicating how many times each experiment was replicated
☐	☒	The statistical test(s) used and whether they are one- or two-sided (note: only common tests should be described solely by name; more complex techniques should be described in the Methods section)
☒	☐	A description of any assumptions or corrections, such as an adjustment for multiple comparisons
☐	☒	The test results (e.g. *P* values) given as exact values whenever possible and with confidence intervals noted
☐	☒	A clear description of statistics including central tendency (e.g. median, mean) and variation (e.g. standard deviation, interquartile range)
☐	☒	Clearly defined error bars

See the web collection on statistics for biologists for further resources and guidance.

▶ Software

Policy information about availability of computer code

7. Software

Describe the software used to analyze the data in this study.

Fiji 2.0 (MosaicSuite, Version November 2016: Particle Tracker 2D/3D), Matlab 2015b (PIVlab 1.41, MSDanalyzer 1.3), AMDIS 0.9 (FEM), Microsoft Excel, Qtiplot 64-bit, LabVIEW 2015 64-bit. All code written in LabVIEW, Matlab or AMDIS is available upon request.

For manuscripts utilizing custom algorithms or software that are central to the paper but not yet described in the published literature, software must be made available to editors and reviewers upon request. We strongly encourage code deposition in a community repository (e.g. GitHub). *Nature Methods* guidance for providing algorithms and software for publication provides further information on this topic.

▶ Materials and reagents

Policy information about availability of materials

8. Materials availability

Indicate whether there are restrictions on availability of unique materials or if these materials are only available for distribution by a for-profit company.

All materials used in this study are available from the authors.

9. Antibodies

Describe the antibodies used and how they were validated for use in the system under study (i.e. assay and species).

No antibodies were used in this study.

10. Eukaryotic cell lines

a. State the source of each eukaryotic cell line used.

S. cerevisiae (W303 MATα can1-100 his3-11,15 leu2-3,112 trp1-1 ura3-1 pAG415GPD-EGFP-μNS) as described in Munder et al., elife 2016 and (W303 MATα can1-100 his3-11,15 leu2-3,112 trp1-1 ura3-1 Ded1-sfGFP-KanMX Pab1-mCherry-HygB) as initially as described by Wallace et al. Cell, 2016, both strains were supplied by the Alberti Lab Dresden.

b. Describe the method of cell line authentication used.

The cells were visually analyzed using a fluorescent microscope for GFP signal and tested by Western Blot for correct protein size.

c. Report whether the cell lines were tested for mycoplasma contamination.

Cell cultures at MPI CBG are routinely checked for contaminations

d. If any of the cell lines used are listed in the database of commonly misidentified cell lines maintained by ICLAC, provide a scientific rationale for their use.

No commonly misidentified cell lines were used.

▶ Animals and human research participants

Policy information about studies involving animals; when reporting animal research, follow the ARRIVE guidelines

11. Description of research animals

Provide details on animals and/or animal-derived materials used in the study.

C. elegans line: TH120 (PAR-2::GFP, PAR-6::mCherry, genotype: unc-119(ed3) III; ddIs25[pie-1::GFP::par-2[RNAi res. SacI/MluI])b + unc-119]; ddIs26[mCherry::T26E3.3 (par-6) + unc-119(+)]) from Schonegg et al., PNAS, 2007 and TH306 (NMY-2::GFP, PAR-2::mCherry, genotype: unc-119(ed3) III; zuIs45[nmy-2::NMY-2::GFP + unc-119(+)] V; ddIs31[pie-1::mCherry::par-2 + unc-119(+)] from Hyman Lab at MPI-CBG, Dresden. LP675 (PAR-2::mNeonGreen, PAR-6::mKate2, genotype: par-6(cp60[par-6::mKate2::3xMyc + LoxP unc-119(+) LoxP]) I; par-2(cp329[mNG^PAR-2]) and SWG007 (lifeact::mKate2; GFP::NMY-2, genotype: nmy-2(cp8 [myo-2::GFP unc-119+]) I; gesIs001 [Pmex-5::Lifeact::mKate::nmy-2UTR, unc-119+]) from Grill Lab at Biotec, TU Dresden

Policy information about studies involving human research participants

12. Description of human research participants

Describe the covariate-relevant population characteristics of the human research participants.

In this study, no human research participants were involved